

EgoVM: Achieving Precise Ego-Localization using Lightweight Vectorized Maps

Yuzhe He Shuang Liang Xiaofei Rui Chengying Cai Guowei Wan*

Baidu Autonomous Driving Technology Department (ADT)

{heyuzhe, liangshuang18, ruixiaofei, caichengying, wanguowei}@baidu.com

Abstract

Accurate and reliable ego-localization is critical for autonomous driving. In this paper, we present EgoVM, an end-to-end localization network that achieves comparable localization accuracy to prior state-of-the-art methods, but uses lightweight vectorized maps instead of heavy point-based maps. To begin with, we extract BEV features from online multi-view images and LiDAR point cloud. Then, we employ a set of learnable semantic embeddings to encode the semantic types of map elements and supervise them with semantic segmentation, to make their feature representation consistent with BEV features. After that, we feed map queries, composed of learnable semantic embeddings and coordinates of map elements, into a transformer decoder to perform cross-modality matching with BEV features. Finally, we adopt a robust histogram-based pose solver to estimate the optimal pose by searching exhaustively over candidate poses. We comprehensively validate the effectiveness of our method using both the nuScenes dataset and a newly collected dataset. The experimental results show that our method achieves centimeter-level localization accuracy, and outperforms existing methods using vectorized maps by a large margin. Furthermore, our model has been extensively tested in a large fleet of autonomous vehicles under various challenging urban scenes.

1. Introduction

Online high-definition (HD) maps derived from bird's eye view (BEV) models have been examined by several studies [23, 32, 28]. However, these maps may suffer from stability and robustness issues due to obstacle occlusions, road abrasion, and inadequate model capabilities, etc., which cannot meet the high quality standards of fully autonomous driving. Therefore, HD maps remain an indispensable component of fully autonomous vehicles as they can provide comprehensive and detailed information about road infrastructure. To utilize HD maps as priors,

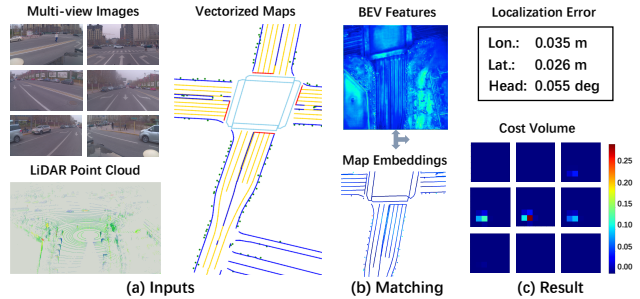


Figure 1. The illustration of our method. (a) The inputs consist of multi-view images, LiDAR point cloud and vectorized maps. (b) The BEV feature extraction module extracts BEV features, which are then interacted with vectorized maps to generate map embeddings by the cross-modality matching module. (c) The pose solver module takes BEV features and map embeddings as inputs and accomplishes centimeter-level localization.

centimeter-level ego-localization is necessary [1].

Several methods have achieved this goal with the aid of 3D light detection and ranging (LiDAR) scanners [18, 21, 22, 58, 59, 17, 53, 30]. In these methods, localization maps are typically represented as points, voxels, or Gaussian distributions on 2D grids, which require enormous storage on the vehicle. This poses significant challenges to deploy the map covering vast areas onto the vehicle. To reduce the map size, several works propose to use pole-like objects [46, 3], vertical corners [13], or footprints and surfaces [14] of buildings as map features. Most of the camera-based methods [60, 43, 51, 61, 37, 15, 9, 56, 42, 7, 39, 55, 27] depend on HD maps that contain lane lines, road markings, poles, traffic signs, etc. Despite the significant progress made by these methods over the years, they still fall behind LiDAR-based techniques in terms of performance. End-to-end localization networks [4, 34, 57, 36, 66] have demonstrated their potential for enhancing localization accuracy, scene generalization, and map compression in recent years. However, these networks also face some limitations, such as the large map size [4, 34], the model-map dependency [57, 66], and the only applicability for simple scenes [36].

A practical localization system for fully autonomous driving should meet the following requirements. First, it should achieve **high accuracy**, with the horizontal localiza-

* Author to whom correspondence should be addressed

tion error and the heading error being within a few centimeters and a few tenths of a degree, respectively. Second, it should ensure **high reliability**, with the ability to maintain centimeter-level accuracy in various complex urban scenes. Third, it should have **good scalability**, with the capability to generate and update the localization map efficiently and massively. Moreover, the localization map should have low storage demand to enable onboard deployment, and the model should be upgradeable without updating the map.

To achieve the above goals, we propose a novel ego-localization network, dubbed **EgoVM (Ego-localization using Vectorized Maps)**. EgoVM takes multi-view images from surrounding cameras, 3D points from LiDAR sensor, and offline vectorized maps as inputs, and estimates the pose offset relative to the initial pose in an end-to-end manner. Figure 1 shows the illustration of our method. In our method, we only estimate 2D position and heading offsets of a 6-Dof pose as in [22, 58, 53]. Generating BEV features from multi-view images, 3D LiDAR points or both has been applied in 3D object detection [26, 33] and semantic segmentation [38, 65]. Therefore, we attempt to perform matching between vectorized maps and BEV features to estimate 3-DoF pose (2D position and heading) offset in BEV space. However, they are still different modalities and difficult to compare, even if they are transformed into a canonical view. To address this issue, we employ a set of learnable embeddings to describe the *semantic types* of vectorized map elements, which include *lane line*, *pedestrian crossing*, *road marking*, *pole* and *traffic sign*, etc. The learnable embeddings are supervised by semantic segmentation to make their features consistent with BEV features. Then, vectorized map elements, represented by learnable semantic embeddings and geometric coordinates, interact with BEV features through a transformer decoder for cross-modality matching. Finally, we apply a robust histogram-based pose solver [4, 34] to determine the optimal pose offset by searching exhaustively over 3-DoF candidate poses.

In summary, our main contributions are:

- An end-to-end localization network that uses light vectorized maps, which achieves centimeter-level localization accuracy comparable to those methods that use heavy point-based maps and is far superior to existing methods that use vectorized maps.
- A novel design for cross-modality matching, which adopts a set of learnable semantic embeddings and a transformer decoder to bridge the representation gap between vectorized maps and BEV features.
- Comprehensive tests and detailed ablation analysis on real-world datasets to verify the effectiveness of the proposed method.
- Integration with other sensors (GNSS, IMU) for a multi-sensor fusion localization system that has been extensively tested in various challenging urban scenes.

2. Related Work

Localization Using Point-based Maps. Methods that align multiple passes of LiDAR point clouds over the same area to construct accurate maps and match the online sensory input with the map have been widely used in fully autonomous vehicles. The pioneering works [21, 22] represent maps using LiDAR intensities, which could provide texture information about the environment. Subsequent works [17, 53] combine altitude information with intensities to achieve more robust and accurate localization. The work of R. Wolcott *et al.* [58, 59] employs Gaussian Mixture Model (GMM) to describe intensity and altitude information, which works well in snowy scenes and has the potential to handle overpass situations. H. Liu *et al.* [30] proposes to extract low-level semantic segmentation-based features, including ground, road-curb, surface, and edge. These methods have achieved impressive performance, but their high storage requirements limit their applicability.

Localization Using Vectorized Maps. A compact representation can be achieved by utilizing lightweight vectorized maps, which contain geometric and semantic information of the scene, such as lane lines [47, 8, 51], road markings [44, 60, 16, 49, 35, 42], poles [48], traffic signs [43], and their combinations [63, 37, 7, 61, 9, 56]. In the case of lane lines and road markings, the matching process can be performed either from perspective or from bird’s eye view. The majority of methods perform matching from perspective view when poles or traffic signs are involved. Several recent methods propose using coarse-to-fine strategy [9], distance transform [37], or robust data association [56, 7] to improve the robustness and availability of localization systems. Our method aims to incorporate vectorized maps to achieve accurate and reliable centimeter-level localization for fully autonomous driving due to their compactness.

End-to-end Localization Networks. End-to-end localization networks that compute similarity between online LiDAR sweeps and intensity map [4] or keypoint map [34] have been explored. They both apply a 3D cost volume to estimate horizontal and heading offsets in an exhaustive searching way. A similar solution [66] exploits long-term salient, distinctive, and stable features to achieve centimeter-level visual localization. X. Wei *et al.* [57] proposes to learn to compress the map without loss of localization accuracy. However, due to deep features residing in the map, the map must be updated for model upgrades, which does not facilitate map deployment and model iteration. W. Ma *et al.* [36] exploits lanes and traffic signs to localize against a sparse semantic map that requires orders of magnitude less storage than previous approaches. Zhang *et al.* [64] proposes an end-to-end visual localization method based on HD Map and BEV representation, similar but different from ours.

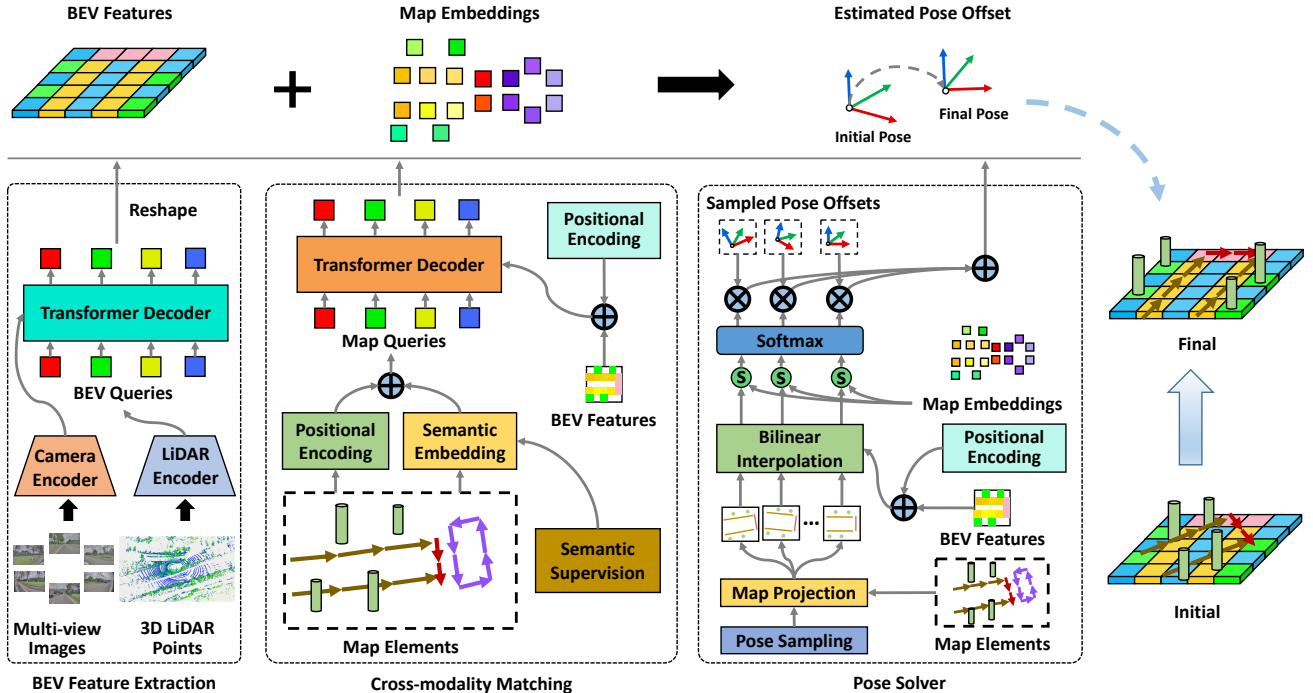


Figure 2. The network architecture of EgoVM. First, the multi-view images and 3D LiDAR points are fed into camera encoder and LiDAR encoder respectively, and fused to obtain BEV features. Second, vectorized map elements and BEV features are used as the queries and keys / values of the transformer decoder for cross-modality matching, thus generating map embeddings. Third, map embeddings are compared with interpolated map features by candidate poses to calculate their similarities, so as to estimate the optimal pose offset.

BEV Feature Extraction. Since prediction and planning tasks operate under bird’s eye view, many methods have attempted to generate BEV features from multi-view images and perform perception task. One series of methods first performs monocular depth estimation, and then lifts 2D image features to 3D space and splats to BEV [41, 45, 11, 12, 24]. Another series of methods employs transformer [50] to perform view transformation [26, 62, 31, 38, 65]. There are also several LiDAR-camera fusion strategies. One is point decoration fusion, which acquires image features or semantic scores for LiDAR points and then generates BEV features, *e.g.*, PointPainting [52], PointAugmenting [54]. A second approach is to fuse the LiDAR BEV features and image BEV features directly under the BEV representation, *e.g.*, BEVFusion [33]. The last kind adopts transformer to perform multi-modality fusion, *e.g.*, DeepFusion [25], TransFusion [2].

3. Problem Formulation

Our goal is to estimate an optimal pose offset given an online point cloud, multi-view images, pre-built vectorized maps, and an initial pose. The pre-built maps contain vectorized elements such as lane lines, road boundaries, pedestrian crossings, stop lines, road markings, traffic signs, and poles, denoted as $M_i | i = 1, 2, \dots, K$, where $M_i \in \mathbb{R}^{m_i}$ is the i -th vectorized map element. Specifi-

cally, lane line, road boundary and stop line are described as horizontal segment on the BEV plane, expressed as endpoints $(x_s, y_s, x_e, y_e) \in \mathbb{R}^4$. The pedestrian crossing is represented by segments of adjacent endpoints of a polygon with $(x_i, y_i, x_{i+1}, y_{i+1}) \in \mathbb{R}^4$. The traffic sign and pole are vectorized as $(x, y, 0, h) \in \mathbb{R}^4$, where (x, y) and h are the center point and height, respectively. Our model also takes an initial pose as an input, which can be provided by a multi-sensor fusion localization system. The estimated pose offset only consists of the 2D horizontal and heading offsets represented as $\Delta T = (\Delta x, \Delta y, \Delta \psi)$, following classical LiDAR-based localization methods [22, 58, 53].

4. Method

Figure 2 shows the three parts of EgoVM. First, the multi-view image features and LiDAR BEV features are extracted and fused into unified BEV features (Section 4.1). Second, a set of learnable embeddings encoding map element types, supervised by semantic segmentation, interact with BEV features through a transformer decoder to perform cross-modality matching, thus obtaining map embeddings (Section 4.2). Third, the pose solver samples several candidate poses to project map elements to BEV plane, obtaining corresponding features by bilinear interpolation, and then compares them with map embeddings to estimate the optimal pose offset (Section 4.3).

4.1. BEV Feature Extraction

We adopt a transformer decoder for fusing image features and LiDAR BEV features. First, multi-view images and LiDAR points are fed into a camera encoder and a LiDAR encoder to extract image features and LiDAR BEV features respectively. Then, the transformer decoder takes LiDAR BEV features to initialize BEV queries and interact with image features, thus obtaining fused BEV features.

Camera Encoder. The multi-view images $\{I_i | i = 1, 2, \dots, N\}$ are fed into a shared backbone network (e.g., ResNet[10], VoVNet[20]), followed by FPN [29] to extract multi-scale features, denoted as $F^I = \{F_{ij}^I | i = 1, 2, \dots, N, j = 1, 2, \dots, L\}$, where $F_{ij}^I \in \mathbb{R}^{H_j \times W_j \times C}$ is the j -th level feature of i -th camera, and H_j, W_j are the height and width of j -th level feature respectively.

LiDAR Encoder. The 3D LiDAR points $\{P_i | i = 1, 2, \dots, n\}$ are first fed into a pillar-based feature extractor (e.g., Pillar Feature Net of PointPillars [19]) to extract pseudo image features. Then, a group of 2D convolutional layers is applied to obtain LiDAR BEV features $F^L \in \mathbb{R}^{H \times W \times C}$ from the pseudo image features, where H and W are the height and width of BEV space.

BEV Fusion. To generate unified LiDAR-camera BEV features, we adopt a transformer decoder to fuse LiDAR BEV features and multi-view image features based on BEVFormer [26]. Specifically, we use LiDAR BEV features to initialize BEV queries, perform self-attention on them, and then apply cross-attention to aggregate multi-view image features. The self-attention and cross-attention layers are implemented based on deformable attention [67] for efficiency. The fused BEV features are denoted as $F^B \in \mathbb{R}^{H \times W \times C}$.

4.2. Cross-modality Matching

Vectorized map elements differ significantly from BEV features in terms of representation. To match them, we employ a set of learnable embeddings and a transformer decoder to bridge the representation gap. The learnable embeddings encode the semantic types of the map elements and then act as queries for the transformer decoder to interact with BEV features and generate unified features for map elements, denoted as *map embeddings*.

Semantic Embedding. Vectorized map elements have different semantic types, such as *lane line*, *road boundary*, *stop line*, *pedestrian crossing*, *road marking*, *pole* and *traffic sign*. We use a set of learnable embeddings $E^{sem} = \{E_j^{sem} \in \mathbb{R}^C | j = 1, 2, \dots, N_e\}$, each of which is expected to learn a specific representation of the corresponding semantic type. Each map element M_i has a semantic type of $s_i \in \{1, 2, \dots, N_e\}$ and a correspondence semantic embedding is $E_{s_i}^{sem} \in E^{sem}$.

Positional Encoding. Vectorized map elements $\{M_i | i = 1, 2, \dots, K\}$ are commonly represented in a global coordinate system, such as Universal Transverse Mercator (UTM) coordinate. First, we normalize them by:

$$\widehat{M}_i = (M_i - O_{xy}) / R_{xy}, \quad (1)$$

where O_{xy} is the initial pose coordinates, and R_{xy} is the height and width ranges of the BEV space.

Then, we feed the normalized map elements $\{\widehat{M}_i\}$ into a shared Multi-Layer Perceptron (MLP) layer to obtain positional encodings $E^{pos} = \{E_i^{pos} \in \mathbb{R}^C | i = 1, 2, \dots, K\}$.

Matching. We apply a transformer decoder to match map elements to BEV features, resulting in *map embeddings* $M^{emb} = \{M_i^{emb} | i = 1, 2, \dots, K\}$. We initialize the map query $Q_i \in \mathbb{R}^C (1 \leq i \leq K)$ of the map element M_i by adding its semantic embedding and positional encoding:

$$Q_i = E_i^{pos} + E_{s_i}^{sem}. \quad (2)$$

The self-attention module of the transformer decoder is formulated as:

$$\text{SA}(Q_i) = \sum_{m=1}^M W_m \sum_{i'=1}^K A_m(Q_i, Q_{i'}) W_m' Q_{i'}, \quad (3)$$

where M is the number of heads, W_m and W_m' are learnable projection matrices, $A_m(Q_i, Q_{i'})$ is attention weight between map queries Q_i and $Q_{i'}$. The cross-attention module is defined as:

$$\text{CA}(Q_i, F^B) = \text{DA}(Q_i, r_i^B, F^B + B^{pos}), \quad (4)$$

where DA represents deformable attention, $r_i^B \in \mathbb{R}^2$ is a reference point that is acquired by projecting the endpoint of map element M_i to BEV space via the initial pose, and B^{pos} is the 2D positional encodings of BEV space.

Semantic Supervision. To better learn the semantic embeddings E^{sem} , we use an auxiliary network that performs semantic segmentation. We take the j -th semantic type as example. The semantic probabilities $S_j \in \mathbb{R}^{H \times W}$ of j -th semantic type with given BEV features F^B is formulated as:

$$S_j(h, w) = \text{sigmoid}(F^B(h, w) \odot E_j^{sem}), \quad (5)$$

where h and w are the indices of BEV grid, and \odot represents dot product.

To generate the ground truth semantic probabilities for each semantic type j , we do the following steps. First, we project the map elements $\{M_i | s_i = j\}$ to the BEV plane using the ground truth pose. Second, we divide the BEV plane into a grid of size $H \times W$ and assign each cell a value of 0 or 1 depending on whether it is occupied by a map element or not. This gives us a binary matrix $S_j^{GT} \in \mathbb{R}^{H \times W}$ that represents the ground truth semantic probabilities for semantic type j .

4.3. Pose Solver

Following [34], we utilize a histogram-based pose solver to estimate the optimal pose offset.

Candidate Poses. We sample candidate pose offsets along x, y and yaw dimensions by grid searching, denoted as $\{\Delta T_{pqr} = (\Delta x_p, \Delta y_q, \Delta \psi_r) | 1 \leq p, q, r \leq N_s\}$, and then generate the candidate poses T_{pqr} by composing the initial pose and them.

Optimal Pose Offset. We project map elements $\{M_i | 1 \leq i \leq K\}$ into the BEV plane using a specific candidate pose T_{pqr} to obtain their BEV features $\{M_i^{bev}(T_{pqr}) | 1 \leq i \leq K\}$ by bilinear interpolation on fused BEV features F^B . Then we calculate the similarity score of F^B and map embeddings M^{emb} under candidate pose T_{pqr} by:

$$S(T_{pqr}) = \frac{1}{K} \sum_{i=1}^K h(M_i^{bev}(T_{pqr}) \odot M_i^{emb}), \quad (6)$$

where $M_i^{emb} \in M^{emb}$ is the map embedding of M_i , and h is a shared MLP. Then, we normalize the similarity scores $\{S(T_{pqr}) | 1 \leq p, q, r \leq N_s\}$ of all candidate poses by *softmax* to obtain the posterior probability $p(T_{pqr}|X)$, where $X = \{F^B, M^{emb}\}$. Finally, we estimate pose offset $\Delta T = E(T|X)$ and covariance $\Sigma = Var(T|X)$ as follows:

$$\Delta T = \sum_{1 \leq p, q, r \leq N_s} p(T_{pqr}|X) \Delta T_{pqr}. \quad (7)$$

$$\Sigma = \sum_{1 \leq p, q, r \leq N_s} p(T_{pqr}|X) (\Delta T_{pqr} - \Delta T) (\Delta T_{pqr} - \Delta T)^T. \quad (8)$$

4.4. Loss Function

RMSE Loss. We define the first loss as the root mean square error (RMSE) between predicted pose offset ΔT and ground truth offset ΔT_{gt} :

$$\mathcal{L}_{rmse} = \|\Lambda^{\frac{1}{2}} U^T (\Delta T - \Delta T_{gt})\|_2, \quad (9)$$

where $\Sigma = USU^T$, and $\Lambda \in \mathbb{R}^{3 \times 3}$ is a diagonal matrix obtained by normalizing the diagonal elements of S^{-1} .

Pose Solver KL loss. The second loss is derived from Kullback-Leibler (KL) divergence $D_{KL}(t(T)||p(T|X))$, which aims to regularize the posterior probability distribution. After dropping constant terms of KL divergence, the KL loss can be obtained:

$$\mathcal{L}_{KL} = - \int t(T) \log p(X|T) dT + \log \int p(X|T) dT, \quad (10)$$

where $t(T)$ and $p(X|T)$ denote the target probability distribution and likelihood function. Note $p(X|T) \propto p(T|X)$, which is defined in the Section 4.3.

Following [6], we define $t(T) = \delta(T - T_{gt})$, and $\delta(\cdot)$ is the Dirac delta function. Equation 10 is rewritten as:

$$\mathcal{L}_{KL} = - \log \frac{\exp(S(T_{gt}))}{\int \exp(S(T)) dT}. \quad (11)$$

Based on this, the pose solver KL loss is obtained by Monte Carlo integration:

$$\mathcal{L}_{KL}^{ps} = - \log \frac{\exp(S(T_{gt}))}{\sum_{1 \leq p, q, r \leq N_s} \exp(S(T_{pqr}))}. \quad (12)$$

Random Pose KL Loss. We use a random pose sampling strategy to enhance the supervision further. The sampled poses $T_j (1 \leq j \leq N_r)$ are drawn from a pose distribution $q(T)$, and the KL loss is calculated as follows:

$$\mathcal{L}_{KL}^{rp} = - \log \frac{\exp(S(T_{gt}))}{\frac{1}{N_r} \sum_{1 \leq j \leq N_r} \frac{1}{q(T_j)} \exp(S(T_j))}, \quad (13)$$

where $q(T)$ is a combination of a 2-DoF multivariate t-distribution on x and y dimensions, and a mixture of von Mises and uniform distribution on yaw dimension.

Semantic Segmentation Loss. We use a semantic segmentation loss function that better supervises semantic embeddings and BEV features by summing up the focal losses (FC) of all semantic classes:

$$\mathcal{L}_{ss} = \sum_{j=1}^{N_e} \text{FC}(S_j, S_j^{GT}). \quad (14)$$

5. Map Extension

Vectorized maps consist of appearance features, such as lane lines, road markings, stop lines, and pedestrian crossings, and geometric features, such as poles and traffic signs. Localization that relies only on appearance features is prone to degradation in low-light conditions. Geometric features can help to improve the localization performance, but they are sparse and not available in every road section. Therefore, we propose to use *surfels* [40][5], which are planar features that are rich in the scene, to enhance the geometric features in the map. We represent surfels as $\{P_i = (p, n, r) \in \mathbb{R}^7\}$, where $p \in \mathbb{R}^2$ is the center point, $n \in \mathbb{R}^3$ is the norm vector, $r = (\lambda_1/\lambda_2, \lambda_1/\lambda_3)$, and $\lambda_1 < \lambda_2 < \lambda_3$ are the eigenvalues of the covariance matrices of surfels. Surfels are abundant and beneficial for localization, but processing all of them is inefficient. Therefore, we apply eigenvalue and grid sampling filters to reduce the number of surfels, by discarding surfels with $\lambda_1/\lambda_2 > 0.1$ and retaining only one surfel with the smallest λ_1/λ_2 in each 1m grid. Like the other vectorized map elements, surfels are involved in the cross-modality matching module to interact with BEV features, and in the pose solver module to estimate the pose.

Method	Longitudinal Error			Lateral Error			Yaw Error		
	MAE(m)	RMSE(m)	<0.1m/0.2m/0.3m(%)	MAE(m)	RMSE(m)	<0.1m/0.2m/0.3m(%)	MAE(°)	RMSE(°)	<0.1°/0.3°/0.6°(%)
MSF-LiDAR	0.041	0.052	<u>94.31/99.86/99.99</u>	0.045	0.058	<u>91.22/99.84/99.99</u>	0.092	0.122	<u>64.02/97.22/99.96</u>
DA4AD	0.089	0.200	76.20/94.14/96.89	0.085	0.167	74.85/93.95/97.06	0.137	0.231	53.56/92.76/98.14
Structure-based	0.318	0.372	14.66/31.26/49.72	0.143	0.191	47.85/74.51/87.74	0.206	0.267	35.33/72.15/97.92
Ours (Visual)	0.149	0.241	45.91/77.43/91.30	0.073	0.098	72.94/95.85/99.52	0.168	0.215	35.75/86.11/99.02
Ours	0.035	<u>0.087</u>	<u>96.94/99.70/99.78</u>	0.033	0.043	97.44/99.93/99.99	0.080	0.106	70.27/98.91/99.89

Table 1. Comparison of localization accuracy with other methods on the self-collected dataset in terms of longitudinal, lateral and heading errors. The best and second best results are highlighted in bold and underline, respectively.

6. Experiments

6.1. Datasets

We evaluate the performance of the proposed network on two datasets: nuScenes and a newly self-collected dataset. The nuScenes dataset contains more than 28,000 frames for training and 6,000 frames for validation. The self-collected dataset consists of 203,645 frames for training and 81,877 frames for validation. Each frame includes six camera images and one LiDAR point cloud, which are time-aligned, as well as intrinsics and extrinsics, ground truth pose and surrounding map elements.

6.2. Performance

Comparison Methods. We compare our method with several state-of-the-art methods, namely MSF-LiDAR [53], DA4AD [66], a structure-based method and BEV-Locator [64]. MSF-LiDAR is a LiDAR-based localization method that models the map as Gaussian distributions on 2D BEV grids. DA4AD is an end-to-end visual localization method that leverages a dense 3D feature point map as the prior. The structure-based method is a visual localization method that matches the 3D landmarks in the HD Map with the perceived 2D landmarks in the online images. BEV-Locator is an end-to-end visual localization method that shares some similarities with ours. However, our method differs from it in several aspects such as map query type, semantic supervision, pose solver and so on. Our method has two modes: visual and full. The visual mode only uses camera images as the input, while the full mode uses both camera images and LiDAR point cloud.

Self-Collected Dataset. We conduct experiments on the self-collected dataset and compare our method with MSF-LiDAR, DA4AD and the structure-based method. The comparison results are shown in Table 1. The localization accuracy is measured by mean absolute error (MAE), root mean square error (RMSE) and the percentage of localization error within a certain threshold (e.g., 0.1m/0.1°). Our method achieves the best MAEs of 0.035m, 0.033m and 0.080° in the longitudinal, lateral and yaw dimensions, respectively, which are superior to the other methods, and the RMSEs of our method are also better than the other methods in the lateral and yaw dimensions. In addition, the percentages of longitudinal, lateral and yaw errors less than

0.3m/0.3m/0.6° are above 99.7%, which indicates the high stability of our method. Compared with DA4AD, the visual mode of our method achieves higher accuracy in the lateral dimension and similar performance in the yaw term. Although the structure-based method and our visual mode both take HD Map and images as inputs, the performance of our visual mode surpasses that of the structure-based method in all evaluation metrics. However, we also notice that the percentage of longitudinal error less than 0.3m of our method is 99.78%, which is lower than that of MSF-LiDAR and the visual mode of our method is also inferior to DA4AD in the longitudinal dimension. The reason is that in some scenarios, there are few landmarks that provide longitudinal constraints in the map, such as poles and signs, as well as surfels, and then our method degrades in the longitudinal dimension. We intend to further explore some new geometric and texture features in our future work.

NuScenes Dataset. As shown in Table 2, we compare our visual mode, full mode and BEV-Locator on the nuScenes dataset. The visual mode of our method achieves lower errors of 0.151m, 0.047m, and 0.092° in the longitudinal, lateral and yaw dimensions, respectively, than those of BEV-Locator, which demonstrates the effectiveness of our visual localization method based on HD Map and images. Furthermore, our full mode improves the localization accuracy by incorporating LiDAR point cloud.

Method	Longitudinal Error		Lateral Error		Yaw Error	
	MAE(m)	<0.3m(%)	MAE(m)	<0.3m(%)	MAE(°)	<0.6°(%)
BEV-Locator	0.178	-	0.076	-	0.510	-
Ours (Visual)	0.151	86.96	0.047	99.64	0.092	99.46
Ours	0.109	94.55	0.034	99.86	0.089	99.50

Table 2. Accuracy evaluation results on the nuScenes dataset.

Localization Map Size	MSF-LiDAR	DA4AD	Ours
MB/km	8.36	5.92	0.35

Table 3. The map sizes of comparison methods.

Map Size. Table 3 reports the map sizes of MSF-LiDAR, DA4AD and our method, which are 8.36MB/km, 5.92MB/km, and 0.35MB/km, respectively. Compared with MSF-LiDAR and DA4AD, our method achieves significant map size reduction by 95.8% and 94.1%, respectively, which demonstrates the compactness of our map.

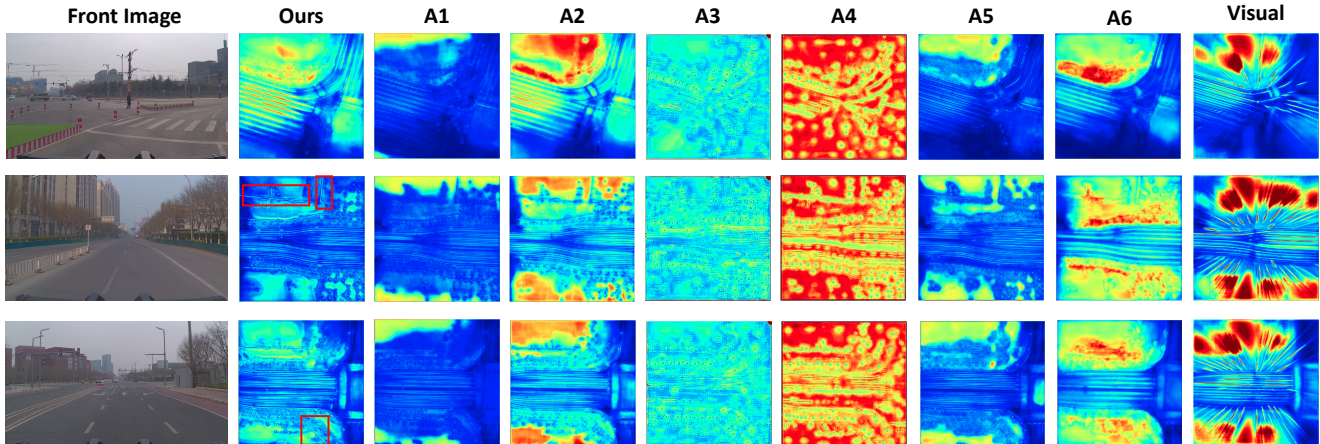


Figure 3. The three rows illustrate the visualization results of three distinct scenes. The leftmost column displays the front images of different scenes, and the remaining columns depict the BEV features of the ablation experiments and the two modes of our method.

	Surfel	Decoder	SemSup	SemEmb	\mathcal{L}_{KL}^{TP}	Histogram	Longitudinal Error			Lateral Error			Yaw Error		
							MAE(m)	RMSE(m)	<0.1m(%)	MAE(m)	RMSE(m)	<0.1m(%)	MAE(°)	RMSE(°)	<0.1°(%)
Ours	✓	✓	✓	✓	✓	✓	0.045	0.121	93.68	0.040	0.059	94.45	0.108	0.136	53.44
A1	✗	✓	✓	✓	✓	✓	0.092	0.298	90.09	0.044	0.102	93.10	0.109	0.144	53.36
A2	✗	✗	✓	✓	✓	✓	0.093	0.317	83.63	0.068	0.223	86.64	0.115	0.176	52.80
A3	✗	✓	✗	✓	✓	✓	0.094	0.345	89.23	0.057	0.227	92.81	0.123	0.168	49.83
A4	✗	✓	✗	✗	✓	✓	0.099	0.384	89.91	0.050	0.157	92.80	0.157	0.225	44.84
A5	✗	✓	✓	✓	✗	✓	0.093	0.350	89.35	0.049	0.132	91.74	0.121	0.156	48.93
A6	✗	✓	✓	✓	✓	✗	0.116	0.352	77.70	0.085	0.266	83.09	0.161	0.310	45.58

Table 4. Ablation experiments of the key components of our method on the augmented self-collected dataset.

6.3. Ablations

To evaluate the effectiveness of each component of our method, we perform several ablation studies on our self-collected dataset. Specifically, to verify the robustness of our method, we randomly remove some types of landmarks from the map with different probabilities in this section. The results are shown in Table 4.

Surfel. In experiment A1, we remove the surfel landmarks from the map. The errors of A1 are higher than those of our full mode, especially in the longitudinal direction. This is because after we randomly remove the pole features in some frames, the longitudinal constraints in these frames can only rely on the surfel features, and the removal of surfel features in A1 experiment will reduce the longitudinal localization accuracy. This demonstrates the effectiveness of the extended surfel features.

Transformer Decoder. Based on A1, we remove the transformer decoder and directly use the map queries as the map embeddings in the experiment A2. The results show that A2 has larger errors than A1, especially in the lateral direction. This indicates that the self-attention of the map queries and the cross-attention of the map queries and the BEV features in the transformer decoder are crucial for our network.

Semantic Ablations. We remove the semantic supervision (SemSup) from A1 in the experiment A3, and we further replace the semantic embeddings (SemEmb) with semantic

encodings as in BEV-Locator in the experiment A4. The results show that A3 and A4 both have larger errors than A1, particularly in the lateral direction. This shows that our network benefits from the combination of semantic embeddings and semantic supervision.

Random Pose KL Loss. The purpose of experiment A5 is to test the effectiveness of our proposed random pose KL loss \mathcal{L}_{KL}^{TP} . Compared with A1, the localization errors of A5 increase for all evaluation metrics, which shows that the random pose KL loss can improve the performance.

Pose Solver. We conduct the experiment A6 to examine the effect of the histogram-based pose solver, in which we use a regression-based pose solver instead of the histogram-based one in A1. The accuracy of the regression-based approach is lower than that of A1. Moreover, the regression-based pose solver lacks interpretability and is hard to debug.

BEV Feature Maps Visualization. To better understand the contribution of each key component, we visualize the BEV features of different modes and ablations of our method. Figure 3 shows the front image and the BEV features. It can be observed that the BEV features of ours, A1, A2, A5, A6 and visual mode with semantic segmentation supervision have clear semantic elements such as lanes, curbs, crosswalks and poles, while the BEV features of A3 and A4 are blurry. This indicates that the semantic supervision enhances the quality and interpretability of the BEV features. Moreover, surfel features (e.g. building surfaces)

Method	AR	Longitudinal Error			Lateral Error			Yaw Error		
		MAE(m)	RMSE(m)	<0.1m/0.2m/0.3m(%)	MAE(m)	RMSE(m)	<0.1m/0.2m/0.3m(%)	MAE(°)	RMSE(°)	<0.1°/0.3°/0.6°(%)
GNSS-RTK	93.67%	0.132	1.082	91.41/93.33/94.12	0.122	0.950	91.26/93.63/94.54	-	-	-
EgoVM	99.82%	0.037	0.104	96.99/99.66/99.77	0.026	0.035	98.54/99.93/99.99	0.131	0.506	42.49/96.29/99.75
Fusion	100.0%	0.030	0.040	97.80/99.84/99.96	0.026	0.036	97.90/99.89/100.0	0.122	0.192	44.41/97.31/99.74

Table 5. Road testing evaluation of localization accuracy over 16,500 km in a test area with road network exceeding 1000 km.

Method	Scene	Longitudinal Error			Lateral Error			Yaw Error		
		MAE(m)	RMSE(m)	<0.1m/0.2m/0.3m(%)	MAE(m)	RMSE(m)	<0.1m/0.2m/0.3m(%)	MAE(°)	RMSE(°)	<0.1°/0.3°/0.6°(%)
Ours (Visual)	Day	0.126	0.199	49.87/81.27/94.98	0.057	0.077	83.92/98.44/99.54	0.184	0.217	26.37/84.64/99.66
	Night	0.160	0.365	46.95/79.06/91.80	0.078	0.108	72.41/95.26/99.01	0.238	0.301	24.61/69.46/96.49
Ours	Day	0.032	0.041	97.95/100.0/100.0	0.029	0.036	99.38/100.0/100.0	0.088	0.114	66.44/97.88/100.0
	Night	0.036	0.045	97.24/99.91/99.99	0.032	0.051	97.39/99.25/99.49	0.116	0.158	55.13/95.18/99.60

Table 6. Evaluation of localization accuracy for the two modes of our method on the day-night dataset.

are also distinctly learned in the BEV features of our full mode marked by red rectangular boxes. In contrast, the BEV features of the visual mode have inaccurate pole positions due to the erroneous depth estimation, which accounts for the large longitudinal error of the visual mode.

6.4. Road Testing Evaluation

We build a multi-sensor fusion localization system based on error-state kalman filter (ESKF) that integrates EgoVM, GNSS-RTK, and inertial navigation, and deploy it to a fleet of RoboTaxi vehicles for road testing evaluation. We tested our localization system in a complex urban area with over 1000 kilometers of road network. By the time of paper submission, our system achieved zero disengagements in autonomous mode for more than 1500 kilometers. Moreover, we verified the robustness and accuracy of our system by running it in open-loop mode for over 15,000 kilometers before switching to autonomous mode. Table 5 compares the localization accuracy of GNSS-RTK, EgoVM and fusion methods. We use four metrics: mean absolute error (MAE), root mean square error (RMSE), percentage of errors within certain thresholds, and available ratio (AR). AR is a new metric that measures the percentage of cases where the longitudinal, lateral and yaw errors are simultaneously less than 0.6m, 0.3m and 1° respectively. The fusion method achieves 100% AR by combining the measurements of GNSS-RTK and inertial navigation, while EgoVM sometimes fails to provide accurate longitudinal localization due to the lack of landmarks in some degraded scenes.

6.5. Night Scenes Evaluation

To test the robustness of our method under low-light conditions, we create another day-night dataset on the same roads. We report the localization errors of the full mode and visual mode of our method in Table 6. The full mode achieves top performance with the aid of LiDAR point cloud, while the visual mode performs poorly in the night scenes due to the low visibility. Figure 4 shows the visualization results, where the first and second row display the day and night scenes, respectively. Each column shows the

front image, the rear image, and the BEV features of the two modes, respectively. The front images reveal that the two scenes are at the same location with different illumination. The BEV features of our full mode show clear lanes in the day scene but blurry lanes in the night scene, however, the poles and surfels are distinctly visible in both scenes marked by yellow and red boxes, ensuring the localization accuracy of our full mode. The BEV features of our visual mode show blurry lanes in the night scene and thus the localization accuracy deteriorates.



Figure 4. Visualization results on the day-night dataset. The first row displays the images and the BEV features of the full mode and visual mode of our method in a day scene. The second row shows the visualization results in a night scene at the same location.

7. Conclusion

We have proposed EgoVM, a novel end-to-end localization network that can improve localization accuracy to the centimeter level with lightweight vectorized maps in various challenging urban scenes. We design a cross-modality matching module comprising learnable semantic embeddings supervised by semantic segmentation and a transformer decoder, which enhances the matching performance by transforming the two input modalities into a unified representation. Moreover, we further improve the localization performance by incorporating LiDAR geometric features, which compensate for the deficiency of appearance features in certain scenes. We have integrated our model with GNSS and IMU sensors to form a multi-sensor fusion localization system and have deployed it to a large fleet of autonomous vehicles, demonstrating its commercial viability.

References

- [1] Claudine Badue, Rânik Guidolini, Raphael Vivacqua Carneiro, Pedro Azevedo, Vinicius B. Cardoso, Avelino Forechi, Luan Jesus, Rodrigo Berriel, Thiago M. Paixão, Filipe Mutz, Lucas de Paula Veronese, Thiago Oliveira-Santos, and Alberto F. De Souza. Self-driving cars: A survey. *Expert Systems with Applications*, 165:113816, 2021. [1](#)
- [2] Xuyang Bai, Zeyu Hu, Xinge Zhu, Qingqiu Huang, Yilun Chen, Hongbo Fu, and Chiew-Lan Tai. TransFusion: Robust lidar-camera fusion for 3d object detection with transformers. In *Proceedings of the IEEE/CVF Conference on Computer Vision and Pattern Recognition (CVPR)*, pages 1090–1099, June 2022. [3](#)
- [3] Tiago Barros, Luís Garrote, Ricardo Pereira, Cristiano Premebida, and Urbano J. Nunes. Improving localization by learning pole-like landmarks using a semi-supervised approach. In Manuel F. Silva, José Luís Lima, Luís Paulo Reis, Alberto Sanfeliu, and Danilo Tardioli, editors, *Robot 2019: Fourth Iberian Robotics Conference*, pages 255–266, Cham, 2020. Springer International Publishing. [1](#)
- [4] Ioan Andrei Bârsan, Shenlong Wang, Andrei Pokrovsky, and Raquel Urtasun. Learning to localize using a lidar intensity map. In *Proceedings of the 2nd Conference on Robot Learning (CoRL)*, 2018. [1](#), [2](#)
- [5] Jens Behley and Cyrill Stachniss. Efficient surfel-based slam using 3d laser range data in urban environments. In *Robotics: Science and Systems*, volume 2018, page 59, 2018. [5](#)
- [6] Hansheng Chen, Pichao Wang, Fan Wang, Wei Tian, Lu Xiong, and Hao Li. EPro-PnP: Generalized end-to-end probabilistic perspective-n-points for monocular object pose estimation. In *Proceedings of the IEEE/CVF Conference on Computer Vision and Pattern Recognition (CVPR)*, pages 2771–2780, 2022. [5](#)
- [7] Wentao Cheng, Sheng Yang, Maomin Zhou, Ziyuan Liu, Yiming Chen, and Mingyang Li. Road mapping and localization using sparse semantic visual features. *IEEE Robotics and Automation Letters (RAL)*, 6(4):8118–8125, 2021. [1](#), [2](#)
- [8] Dixiao Cui, Jianru Xue, Shaoyi Du, and Nanning Zheng. Real-time global localization of intelligent road vehicles in lane-level via lane marking detection and shape registration. In *Proceedings of the IEEE/RSJ International Conference on Intelligent Robots and Systems (IROS)*, 2014. [2](#)
- [9] Chengcheng Guo, Minjie Lin, Heyang Guo, Pengpeng Liang, and Erkang Cheng. Coarse-to-fine semantic localization with hd map for autonomous driving in structural scenes. In *Proceedings of the IEEE/RSJ International Conference on Intelligent Robots and Systems (IROS)*, pages 1146–1153, 2021. [1](#), [2](#)
- [10] Kaiming He, X. Zhang, Shaoqing Ren, and Jian Sun. Deep residual learning for image recognition. *Proceedings of the IEEE Conference on Computer Vision and Pattern Recognition (CVPR)*, pages 770–778, 2016. [4](#)
- [11] Anthony Hu, Zak Murez, Nikhil Mohan, Sofia Dudas, Jeffrey Hawke, Vijay Badrinarayanan, Roberto Cipolla, and Alex Kendall. FIERY: Future instance prediction in bird’s-eye view from surround monocular cameras. *Proceedings of IEEE International Conference on Computer Vision (ICCV)*, 2021. [3](#)
- [12] Junjie Huang, Guan Huang, Zheng Zhu, and Dalong Du. BEVDet: High-performance multi-camera 3d object detection in bird-eye-view. *arXiv preprint arXiv:2112.11790*, 2021. [3](#)
- [13] Jun-Hyuck Im, Sung-Hyuck Im, and Gyu-In Jee. Vertical corner feature based precise vehicle localization using 3d lidar in urban area. *Sensors*, 16(8), 2016. [1](#)
- [14] Ehsan Javanmardi, Yanlei Gu, Mahdi Javanmardi, and Shunsuke Kamijo. Autonomous vehicle self-localization based on abstract map and multi-channel lidar in urban area. *IATSS Research*, 43(1):1–13, 2019. [1](#)
- [15] Jinyong Jeong, Younggun Cho, and Ayoung Kim. HDMLoc: Exploiting high definition map image for precise localization via bitwise particle filter. *IEEE Robotics and Automation Letters (RAL)*, 5(4):6310–6317, 2020. [1](#)
- [16] Kichun Jo, Yongwoo Jo, Jae Kyu Suhr, Ho Gi Jung, and Myoung Sunwoo. Precise localization of an autonomous car based on probabilistic noise models of road surface marker features using multiple cameras. *IEEE Transactions on Intelligent Transportation Systems (T-ITS)*, 2015. [2](#)
- [17] Hyungjin Kim, Bingbing Liu, Chi Yuan Goh, Serin Lee, and Hyun Myung. Robust vehicle localization using entropy-weighted particle filter-based data fusion of vertical and road intensity information for a large scale urban area. *IEEE Robotics and Automation Letters (RAL)*, 2(3):1518–1524, 2017. [1](#), [2](#)
- [18] Rainer Kummerle, Dirk Hahnel, Dmitri Dolgov, Sebastian Thrun, and Wolfram Burgard. Autonomous driving in a multi-level parking structure. In *Proceedings of the IEEE International Conference on Robotics and Automation (ICRA)*, pages 3395–3400, 2009. [1](#)
- [19] Alex H. Lang, Sourabh Vora, Holger Caesar, Lubing Zhou, Jiong Yang, and Oscar Beijbom. PointPillars: Fast encoders for object detection from point clouds. *Proceedings of the IEEE/CVF Conference on Computer Vision and Pattern Recognition (CVPR)*, pages 12689–12697, 2019. [4](#)
- [20] Youngwan Lee and Jongyoul Park. CenterMask: Real-time anchor-free instance segmentation. *Proceedings of the IEEE/CVF Conference on Computer Vision and Pattern Recognition (CVPR)*, pages 13903–13912, 2020. [4](#)
- [21] Jesse Levinson, Michael Montemerlo, and Sebastian Thrun. Map-based precision vehicle localization in urban environments. *Robotics: Science and Systems*, 4:1, 2007. [1](#), [2](#)
- [22] Jesse Levinson and Sebastian Thrun. Robust vehicle localization in urban environments using probabilistic maps. In *Proceedings of the IEEE International Conference on Robotics and Automation (ICRA)*, pages 4372–4378, May 2010. [1](#), [2](#), [3](#)
- [23] Qi Li, Yue Wang, Yilun Wang, and Hang Zhao. HDMapNet: An online hd map construction and evaluation framework. In *Proceedings of the IEEE International Conference on Robotics and Automation (ICRA)*, pages 4628–4634, 2022. [1](#)
- [24] Yin hao Li, Zheng Ge, Guanyi Yu, Jinrong Yang, Zengran Wang, Yukang Shi, Jianjian Sun, and Zeming Li. BEVDepth:

- Acquisition of reliable depth for multi-view 3d object detection. *arXiv preprint arXiv:2206.10092v2*, 2022. 3
- [25] Yingwei Li, Adams Wei Yu, Tianjian Meng, Ben Caine, Jiquan Ngiam, Daiyi Peng, Junyang Shen, Yifeng Lu, Denny Zhou, Quoc V. Le, Alan Yuille, and Mingxing Tan. DeepFusion: Lidar-camera deep fusion for multi-modal 3d object detection. In *Proceedings of the IEEE/CVF Conference on Computer Vision and Pattern Recognition (CVPR)*, pages 17182–17191, June 2022. 3
- [26] Zhiqi Li, Wenhai Wang, Hongyang Li, Enze Xie, Chonghao Sima, Tong Lu, Yu Qiao, and Jifeng Dai. BEVFormer: Learning bird’s-eye-view representation from multi-camera images via spatiotemporal transformers. In *Proceedings of the European Conference on Computer Vision (ECCV)*, 2022. 2, 3, 4
- [27] Shiwen Liang, Yunzhou Zhang, Rui Tian, Delong Zhu, Linghao Yang, and Zhenzhong Cao. SemLoc: Accurate and robust visual localization with semantic and structural constraints from prior maps. In *Proceedings of the IEEE International Conference on Robotics and Automation (ICRA)*, pages 4135–4141, 2022. 1
- [28] Bencheng Liao, Shaoyu Chen, Xinggang Wang, Tianheng Cheng, Qian Zhang, Wenyu Liu, and Chang Huang. MapTR: Structured modeling and learning for online vectorized hd map construction. *arXiv preprint arXiv:2208.14437*, 2021. 1
- [29] Tsung-Yi Lin, Piotr Dollár, Ross Girshick, Kaiming He, Bharath Hariharan, and Serge Belongie. Feature pyramid networks for object detection. In *Proceedings of the IEEE Conference on Computer Vision and Pattern Recognition (CVPR)*, pages 936–944, 2017. 4
- [30] Hang Liu, Qin Ye, Hairui Wang, Liang Chen, and Jian Yang. A precise and robust segmentation-based lidar localization system for automated urban driving. *Remote Sensing*, 11(11), 2019. 1, 2
- [31] Yingfei Liu, Junjie Yan, Fan Jia, Shuailin Li, Qi Gao, Tiancai Wang, Xiangyu Zhang, and Jian Sun. PETRv2: A unified framework for 3d perception from multi-camera images. *arXiv preprint arXiv:2206.01256*, 2022. 3
- [32] Yicheng Liu, Yuan Yuantian, Yue Wang, Yilun Wang, and Hang Zhao. VectorMapNet: End-to-end vectorized hd map learning. *arXiv preprint arXiv:2206.08920*, 2022. 1
- [33] Zhijian Liu, Haotian Tang, Alexander Amini, Xinyu Yang, Huizi Mao, Daniela Rus, and Song Han. BEVFusion: Multi-task multi-sensor fusion with unified bird’s-eye view representation. *CoRR*, abs/2205.13542, 2022. 2, 3
- [34] Weixin Lu, Yao Zhou, Guowei Wan, Shenhua Hou, and Shiyu Song. L3-Net: Towards learning based LiDAR localization for autonomous driving. In *Proceedings of the IEEE Conference on Computer Vision and Pattern Recognition (CVPR)*. IEEE, 2019. 1, 2, 5
- [35] Yan Lu, Jiawei Huang, Yi-Ting Chen, and Bernd Heisele. Monocular localization in urban environments using road markings. In *Proceedings of the IEEE Intelligent Vehicles Symposium (IV)*, 2017. 2
- [36] Wei-Chiu Ma, Ignacio Tartavull, Ioan Andrei Bârsan, Shenlong Wang, Min Bai, Gellert Mattyus, Namdar Homayounfar, Shrinidhi Kowshika Lakshminanth, Andrei Pokrovsky, and Raquel Urtasun. Exploiting sparse semantic hd maps for self-driving vehicle localization. In *Proceedings of the IEEE/RSJ International Conference on Intelligent Robots and Systems (IROS)*, pages 5304–5311, 2019. 1, 2
- [37] Jan-Hendrik Pauls, Kürsat Petek, Fabian Poggenhans, and Christoph Stiller. Monocular localization in hd maps by combining semantic segmentation and distance transform. In *Proceedings of the IEEE/RSJ International Conference on Intelligent Robots and Systems (IROS)*, pages 4595–4601, 2020. 1, 2
- [38] Lang Peng, Zhirong Chen, Zhang-Hua Fu, Pengpeng Liang, and Erkang Cheng. BEVSegFormer: Bird’s eye view semantic segmentation from arbitrary camera rigs. *ArXiv*, abs/2203.04050, 2022. 2, 3
- [39] Kürsat Petek, Kshitij Sirohi, Daniel Büscher, and Wolfram Burgard. Robust monocular localization in sparse hd maps leveraging multi-task uncertainty estimation. In *Proceedings of the IEEE International Conference on Robotics and Automation (ICRA)*, pages 4163–4169, 2022. 1
- [40] Hanspeter Pfister, Matthias Zwicker, Jeroen Van Baar, and Markus Gross. Surfels: Surface elements as rendering primitives. In *Proceedings of the 27th annual conference on Computer graphics and interactive techniques*, pages 335–342, 2000. 5
- [41] Jonah Philion and Sanja Fidler. Lift, splat, shoot: Encoding images from arbitrary camera rigs by implicitly unprojecting to 3d. In *Proceedings of the European Conference on Computer Vision (ECCV)*, 2022. 3
- [42] Tong Qin, Yuxin Zheng, Tongqing Chen, Yilun Chen, and Qing Su. A light-weight semantic map for visual localization towards autonomous driving. In *Proceedings of the IEEE International Conference on Robotics and Automation (ICRA)*, pages 11248–11254, 2021. 1, 2
- [43] Xiaozhi Qu, Bahman Soheilian, and Nicolas Paparoditis. Vehicle localization using mono-camera and geo-referenced traffic signs. In *Proceedings of the IEEE Intelligent Vehicles Symposium (IV)*, pages 605–610, 2015. 1, 2
- [44] Ananth Ranganathan, David Ilstrup, and Tao Wu. Light-weight localization for vehicles using road markings. In *Proceedings of the IEEE/RSJ International Conference on Intelligent Robots and Systems (IROS)*, 2013. 2
- [45] Cody Reading, Ali Harakeh, Julia Chae, and Steven L. Waslander. Categorical depth distribution network for monocular 3d object detection. In *Proceedings of the IEEE Conference on Computer Vision and Pattern Recognition (CVPR)*, 2021. 3
- [46] Alexander Schaefer, Daniel Büscher, Johan Vertens, Lukas Luft, and Wolfram Burgard. Long-term urban vehicle localization using pole landmarks extracted from 3-d lidar scans. In *Proceedings of the European Conference on Mobile Robots (ECMR)*, 2019. 1
- [47] Markus Schreiber, Carsten Knöppel, and Uwe Franke. LaneLoc: Lane marking based localization using highly accurate maps. *Proceedings of the IEEE Intelligent Vehicles Symposium (IV)*, 2013. 2
- [48] Robert Spangenberg, Daniel Goehring, and Raúl Rojas. Pole-based localization for autonomous vehicles in urban

- scenarios. In *Proceedings of the IEEE/RSJ International Conference on Intelligent Robots and Systems (IROS)*, 2016. [2](#)
- [49] Jae Kyu Suhr, Jeungin Jang, Daehong Min, and Ho Gi Jung. Sensor fusion-based low-cost vehicle localization system for complex urban environments. *IEEE Transactions on Intelligent Transportation Systems (T-ITS)*, 2017. [2](#)
- [50] Ashish Vaswani, Noam Shazeer, Niki Parmar, Jakob Uszkoreit, Llion Jones, Aidan N. Gomez, Lukasz Kaiser, and Illia Polosukhin. Attention is all you need. In *Proceedings of the 31st International Conference on Neural Information Processing Systems (NeurIPS)*, 2017. [3](#)
- [51] Rafael Peixoto Derenzi Vivacqua, Massimo Bertozzi, Pietro Cerri, Felipe Nascimento Martins, and Raquel Frizzera Vassallo. Self-localization based on visual lane marking maps: An accurate low-cost approach for autonomous driving. *IEEE Transactions on Intelligent Transportation Systems (T-ITS)*, 19(2):582–597, feb 2018. [1](#), [2](#)
- [52] Sourabh Vora, Alex H. Lang, Bassam Helou, and Oscar Beijbom. PointPainting: Sequential fusion for 3d object detection. In *Proceedings of the IEEE/CVF Conference on Computer Vision and Pattern Recognition (CVPR)*, 2020. [3](#)
- [53] Guowei Wan, Xiaolong Yang, Renlan Cai, Hao Li, Yao Zhou, Hao Wang, and Shiyu Song. Robust and precise vehicle localization based on multi-sensor fusion in diverse city scenes. In *Proceedings of the IEEE International Conference on Robotics and Automation (ICRA)*, page 4670–4677. IEEE Press, 2018. [1](#), [2](#), [3](#), [6](#)
- [54] Chunwei Wang, Chao Ma, Ming Zhu, and Xiaokang Yang. PointAugmenting: Cross-modal augmentation for 3d object detection. In *Proceedings of the IEEE/CVF Conference on Computer Vision and Pattern Recognition (CVPR)*, pages 11794–11803, June 2021. [3](#)
- [55] Huayou Wang, Changliang Xue, Yu Tang, Wanlong Li, Feng Wen, and Hongbo Zhang. LTSR: Long-term semantic relocalization based on hd map for autonomous vehicles. In *Proceedings of the IEEE International Conference on Robotics and Automation (ICRA)*, pages 2171–2178, 2022. [1](#)
- [56] Huayou Wang, Changliang Xue, Yanxing Zhou, Feng Wen, and Hongbo Zhang. Visual semantic localization based on hd map for autonomous vehicles in urban scenarios. In *Proceedings of the IEEE International Conference on Robotics and Automation (ICRA)*, pages 11255–11261, 2021. [1](#), [2](#)
- [57] Xinkai Wei, Ioan Andrei Bârsan, Shenlong Wang, Julieta Martinez, and Raquel Urtasun. Learning to localize through compressed binary maps. In *Proceedings of the IEEE/CVF Conference on Computer Vision and Pattern Recognition (CVPR)*, pages 10308–10316, 2019. [1](#), [2](#)
- [58] Ryan W Wolcott and Ryan M Eustice. Fast LiDAR localization using multiresolution gaussian mixture maps. In *Proceedings of the IEEE International Conference on Robotics and Automation (ICRA)*, pages 2814–2821, May 2015. [1](#), [2](#), [3](#)
- [59] Ryan W Wolcott and Ryan M Eustice. Robust LiDAR localization using multiresolution gaussian mixture maps for autonomous driving. *The International Journal of Robotics Research (IJRR)*, 36(3):292–319, 2017. [1](#), [2](#)
- [60] Tao Wu and Ananth Ranganathan. Vehicle localization using road markings. In *Proceedings of the IEEE Intelligent Vehicles Symposium (IV)*, pages 1185–1190, 2013. [1](#), [2](#)
- [61] Zhongyang Xiao, Diange Yang, Tuopu Wen, Kun Jiang, and Ruidong Yan. Monocular localization with vector hd map (MLVHM): A low-cost method for commercial IVs. *Sensors*, 20(7), 2020. [1](#), [2](#)
- [62] Weixiang Yang, Qi Li, Wenxi Liu, Yuanlong Yu, Yuexin Ma, Shengfeng He, and Jia Pan. Projecting your view attentively: Monocular road scene layout estimation via cross-view transformation. *Proceedings of the IEEE/CVF Conference on Computer Vision and Pattern Recognition (CVPR)*, 2021. [3](#)
- [63] Yufeng Yu, Huijing Zhao, Franck Davoine, Jinshi Cui, and Hongbin Zha. Monocular visual localization using road structural features. In *Proceedings of the IEEE Intelligent Vehicles Symposium (IV)*, 2014. [2](#)
- [64] Zhihuang Zhang, Meng Xu, Wenqiang Zhou, Tao Peng, Liang Li, and Stefan Poslad. BEV-Locator: An end-to-end visual semantic localization network using multi-view images. *arXiv preprint arXiv:2211.14927*, 2022. [2](#), [6](#)
- [65] Brady Zhou and Philipp Krähenbühl. Cross-view transformers for real-time map-view semantic segmentation. In *Proceedings of the IEEE/CVF Conference on Computer Vision and Pattern Recognition (CVPR)*, 2022. [2](#), [3](#)
- [66] Yao Zhou, Guowei Wan, Shenhua Hou, Li Yu, Gang Wang, Xiaofei Rui, and Shiyu Song. DA4AD: End-to-end deep attention-based visual localization for autonomous driving. In *Proceedings of the European Conference on Computer Vision (ECCV)*, page 271–289, 2020. [1](#), [2](#), [6](#)
- [67] Xizhou Zhu, Weijie Su, Lewei Lu, Bin Li, Xiaogang Wang, and Jifeng Dai. Deformable DETR: deformable transformers for end-to-end object detection. In *Proceedings of the 9th International Conference on Learning Representations (ICLR)*, 2021. [4](#)

A. More Details about Network

Network Configurations. We use VoVNet-39 as the image backbone in our experiments. The camera encoder takes images resized to 448×640 as input and outputs a single-layer image feature map of size $28 \times 40 \times 256$. The LiDAR point cloud is cropped to $[-40m, 40m]$ in x-y dimensions and $[-3m, 5m]$ in z dimension before being fed into the LiDAR encoder, which produces LiDAR BEV feature map of size $160 \times 160 \times 256$ and resolution of $0.5m$. Both transformer decoders have four layers. The histogram search range in the pose solver is $[-3m, 3m]$ in x-y dimensions and $[-3^\circ, 3^\circ]$ in yaw dimension.

Multi-Layer BEV Feature Maps. As mentioned above, we set the resolution as $0.5m$ to guarantee the efficiency for extracting BEV feature map. However, $0.5m$ is too coarse to achieve highly accurate localization, therefore, we up-sample the original BEV feature map twice to obtain finer BEV feature maps with resolutions of $0.25m$ and $0.125m$. Meanwhile, we reduce the channel dimensions of the finer-layer BEV feature maps to increase efficiency. Specifically, the sizes of three-layer feature maps $F^{B,0}$, $F^{B,1}$ and $F^{B,2}$ are $160 \times 160 \times 256$, $320 \times 320 \times 128$, $640 \times 640 \times 64$, respectively. In addition, we project original 256 dimensional semantic embeddings to lower dimensions by Conv1Ds and conduct semantic supervision for all three layer BEV feature maps using Equation 5.

Multi-Level Pose Solver. To ensure efficiency, we need to select a proper grid size for the histogram, which has a large search range of $[-3m, 3m]$ in x-y dimensions and $[-3^\circ, 3^\circ]$ in yaw dimension. In practice, we set the grid size as $0.5m$, but this is too large to achieve highly accurate localization results. Therefore, we design an iterative multi-level pose solver that uses two additional histograms with smaller search ranges and grid sizes. The details of multi-level pose solver are described in Algorithm 1.

Map Elements Projection. BEV plane is affected by the rolling and pitching of vehicle platform, whereas vectorized map elements remain in horizontal plane. To match map elements with BEV features, we need to transform map elements into the same coordinate as BEV features. Firstly, we find the z coordinate of the map element’s endpoint by intersecting the vertical line through (x, y) and the BEV space, as illustrated in Figure 5. The intersection of the 2D endpoint (x, y) and the BEV space is denoted by $p = (x, y, z)$ and follows the equation below:

$$n^T(p - t_{WL}) = 0, \quad (1)$$

where $n = R_{WL}(0, 0, 1)^T \triangleq (n_x, n_y, n_z)$ is the unit vector of z-axis of the LiDAR sensor in world frame and the value

Algorithm 1: Multi-Level Pose Solver

Input: BEV feature maps: $\{F^{B,l} | l \in \{0, 1, 2\}\}$;
 Map embeddings: $\{M_i^{emb} | 1 \leq i \leq K\}$;
 Initial pose: T_{init} .
Output: Estimated pose: T_{est} ;
 Estimated pose offset: ΔT_{est} ;
 Covariances: $\{\Sigma_l\}$.

- 1 Initialize $T_{est} = T_{init}, \Delta T_{est} = 0$;
- 2 **for** $l \in \{0, 1, 2\}$ **do**
- 3 Sample pose offsets by grid search,
 $\{\Delta T_{pqr}^l | 1 \leq p, q, r \leq N_s\} \in$
 $[-\frac{r_x}{2^l}, \frac{r_x}{2^l}] \times [-\frac{r_y}{2^l}, \frac{r_y}{2^l}] \times [-\frac{r_{yaw}}{2^l}, \frac{r_{yaw}}{2^l}]$;
- 4 $T_{pqr}^l = T_{est} \oplus \Delta T_{pqr}^l$;
- 5 Unify BEV features and map embeddings,
 $F^{B,l} = Conv2d^l(F^{B,l})$,
 $M_i^{emb,l} = MLP^l(M_i^{emb})$;
- 6 Project map elements to BEV space,
 $p_i^B(T_{pqr}^l) = project(T_{pqr}^l, M_i)$;
- 7 Sample features by bilinear interpolation,
 $M_i^{bev}(T_{pqr}^l) = bi_inter(F^{B,l}, p_i^B(T_{pqr}^l))$;
- 8 Obtain $\Delta T_l, \Sigma_l$ by equation (6), (7), (8);
- 9 $T_{est} = T_{est} \oplus \Delta T_l$;
- 10 $\Delta T_{est} = \Delta T_{est} + \Delta T_l$
- 11 **end**
- 12 **Return** $T_{est}, \Delta T_{est}, \{\Sigma_l | l \in \{0, 1, 2\}\}$

of z is determined as follows:

$$z = \frac{n^T t_{WL} - n_x x - n_y y}{n_z} \quad (2)$$

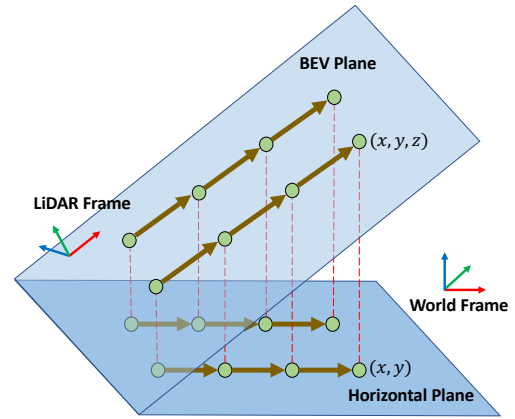


Figure 5. To project map elements, we first intersect vertical lines through the endpoints and the BEV space to get the z coordinates. Then, we transform these 3D points into LiDAR frame and normalize them to obtain their representations in BEV space.

Then we project p from world frame to LiDAR frame:

$$p^L = R_{WL}^T(p - t_{WL}). \quad (3)$$

Finally, we normalize $p^L \triangleq (x^L, y^L, z^L)$ to obtain the coordinate of the end point (x, y) in the BEV space:

$$p^B = \left(\frac{x^L - h_{min}}{r}, \frac{y^L - w_{min}}{r} \right), \quad (4)$$

where h_{min} and w_{min} are the minimum values in the BEV space, and r is the resolution of each BEV grid.

B. More about Training

Data Augmentation. We use two data augmentation tricks in the training stage: LiDAR frame rotation and world frame rotation. For LiDAR frame rotation, we randomly rotate the LiDAR frame by θ around its z-axis and adjust the LiDAR pose, the LiDAR point cloud coordinates and the extrinsics from LiDAR to cameras accordingly. For world frame rotation, we randomly rotate the world frame by ϕ around its z-axis and adjust the LiDAR pose and the vectorized map element coordinates accordingly.

Training Strategy. We train our models on a NVIDIA A100 GPU cluster for 36 epochs with a batch size of 3 for each GPU. We set the base learning rate to 2×10^{-4} . We use an image backbone pretrained on ImageNet with a learning rate multiplier of 0.1 and a cosine annealing decay. We use AdamW optimizer with a weight decay of 0.01.

C. More about Ablations

Augmented Self-collected Dataset. In order to test the significance of each module and increase the localization difficulty, we conduct ablation experiments by dropping some landmarks of the dataset. We use a random process to discard each type of landmark with a certain probability for each frame. Specifically, we set the drop probabilities for pole and curb landmarks to 5% and 50%, respectively.

Regression-based Pose Solver. In ablation experiment A5, we implement a regression-based pose solver instead of our histogram-based pose solver. The regression-based pose solver consists of an encoder block, a max-pooling layer and a MLP. The encoder block consists of three Conv1D(256,256,1) layers, where the first two layers are followed by BatchNorm and ReLU. The MLP consists of three 1D CNN layers: Conv1D(256,1024,1), Conv1D(1024,1024,1), Conv1D(1024,3,1), where the first two layers are followed by ReLU activation functions.

D. More about Self-collected Dataset

Sensor Suite Configuration. The sensor suite on our autonomous vehicle consists of a HESAI Pandar40P LiDAR, six FPD-LINK serial AR0231-AP0202-TI913 cameras and a NovAtel PwrPak7D-E1 integrated navigation system.

Ground Truth Poses Acquisition. Our goal is to obtain the ground truth poses of test frames that are consistent with

vectorized maps. To achieve this, we first construct a large, precise and globally consistent point cloud map using point cloud registration techniques. Then, we generate vectorized maps based on this map. Next, we use GNSS RTK/INS post-processing software like NovAtel Inertial Explorer to get the initial poses of test frames. Finally, we align the test frames to the pre-built point cloud map using point cloud registration techniques again to get their ground truth poses.

E. Run-time Analysis

We test the run-time performance of our method on a GeForce RTX 3080 GPU and a Intel(R) Xeon(R) W-3245 CPU @ 3.20GHz. The run-time statistics of comparison methods are shown in Table 7. Our method has an average processing time of 120.31ms and a maximum processing time of 127.00ms. Although our method is slightly slower than others on average, it still meets the real-time localization requirement. Moreover, our method has a more stable inference time than MSF-LiDAR and DA4AD.

Method	Average(s)	99%(s)	Max(s)
MSF-LiDAR	51.91	111.76	316.00
DA4AD	70.93	76.00	117.00
Ours	120.31	125.00	127.00

Table 7. Run-time statistics of comparison methods.